Control of the light extraction from a photonic crystal nanocavity by coupling with a nanoparticle

Abdullah F. Alabiad[1], Blandine E. Guichardaz[1] and Fadi I. Baida[1]

1 FEMTO-ST Institute, UMR 6174 CNRS, Department of Optics P. M. Duffieux, University of Bourgogne Franche–Comté, 25030 Besançon Cedex, France

E-mail: abdullah.alabiad2@femto-st.fr

Abstract. In this paper, we present a numerical study (using Finite Difference Times Domain (FDTD) method) of the coupling between two resonant structures with different quality factors of their resonances. The first is a Photonic Crystal Cavity (PCC) while the second is a dielectric Nano-Particle (NP). Both structures exhibit optical responses at the same wavelength, which allows a critical coupling between them. The objective of the study is to exploit this coupling to control the light extraction properties of the more resonant structure (the PCC). The challenge is then: first, to model such a near-field coupling through numerical method that can handle the entire structure (PCC+NA) and second, to get physical insight about the interaction allowing a good control of the light extraction. We numerically demonstrate that this coupling strongly depends on the spatial position of the NP relative to the PCC. We also show that the direction of the emission (into the substrate or superstrate) and its intensity can be adjusted by the NP position relative to the PCC. Quantitatively, the critical coupling corresponds to an NP-PCC distance of 120 nm leading to an increase by factor of 3 of the light radiated towards the far field. This is accompanied by a red shift of 0.53 nm of the cavity resonance. This study opens the way to the development of a new kind of sources with both "controllable" wavelength resonance and radiation pattern.

Keywords: Photonic Crystal, Light Extraction Enhancement, Directivity, Radiation Angular Spectrum.

Submitted to: *J. Phys. Commun.*

1. Introduction

The search for techniques to improve the efficiency of light extraction and to manipulate its directivity from sources such that light-emitting diodes (LEDs), Photonic Crystals (PC) or optical nano-antennas (NA), has attracted the attention of researchers in recent years. Some have used a PC as a reflecting layer to improve by a factor of 2.6 [1] the directivity or the efficiency by 47% [2] and, even more, by 70% [3] of the light extraction from thin-film LEDs. Others have experimentally demonstrated that they can increase the light extraction efficiency from a PC up to 70% [4, 5] and up to 8 times higher than non-patterned structure with high directivity of light emitted [6] by changing its geometrical parameters (lattice constant, pattern shape) . On the other hand, some researchers have used optical nano-antennas to control the radiation pattern of given emitters [7–14]. One of them [8] shows a maximum directivity emission up to 3.8 times higher with a rotation change of 90° compared to the free emitter. In another approach, an enhancement factor up to 260 times for the fluerescence efficiency of a PC was experimentally obtained by coupling it with another resonator such as a nanoparticle [15–17].
In all these studies, the configurations are passive because their geometry is fixed and does not allow to modify the coupling properties. Here we bring a first approach to lift this lock by considering a configuration where one of the elements can move relative to the other. Achieving experimentally this flexibility in the configuration will be discussed in the conclusion. For this purpose, we numerically determine the angular radiation spectrum of light extracted from a Photonic Crystal Cavity (PCC) coupled to an Electric Dipolar (ED) resonant Nano-Particle (NP) as a function of its spatial position and demonstrate the possible control of the light emission properties of this combination. First, we present the properties of the PCC which has already been studied theoretically and experimentally by our team [18, 19]. Second, we numerically design a dielectric NP using Mie theory so that its electric dipolar resonance matches the resonance wavelength of the PCC. Third, we calculate, utilizing the FDTD results, the angular spectrum of radiation of the whole system (PCC+NP) both in the substrate and the superstrate with respect to the position of the NP. We demonstrate how to control the light emission direction and energy by moving in the 3 directions the NP with respect to the PCC.

2. Numerical Studies

In the following, we will first study the optical properties of each resonators (PCC, NP) individually and, second, their coupling. Due to the fact that the cavity mode of the considered PCC occurs for a well given value of the wavelength, we design the NP so it presents an electric dipole (ED) resonance at the same wavelength by modifying its refractive index. Let mention that the calculations are done within the Mie theory in the case of self-suspended spherical NP while an adapted TFSF (Total Field Scattered

Field) algorithm [20] is used in the case of NP in the vicinity of dielectric substrate. All these codes are home-made codes as the one used to simulate the NP to PCC coupling.

2.1. Study of the PCC

The considered PCC was proposed since 2003 by Monat et al. [21] to exhibit a cavity mode in the NIR spectral range. It consists on a 2D hexagonal photonic crystal composed of air hole cylinders of radius $r = 105\ nm$ with a lattice constant $a = 420\ nm$. The holes are engraved into an InP layer of 300 nm-thickness deposited on a silica layer of 1 μm-thickness on top of silicone substrate. The optical cavity is composed of seven missed and aligned air holes (then called CL7) as shown in figure 1(a). Note that the two air holes at the extremities of the cavity are offset 75 nm towards the outside of the cavity in order to enhance the quality factor of the cavity mode resonance keeping it inside the photonic bandgap of the PC dispersion diagram. The near-field spectrum calculated 15 nm above the PCC center is shown in figure 1(b). The cavity mode occurs at the wavelength $\lambda_0^{mode} = 1602.92\ nm$ with a quality factor of $Q_0 = 4035$ as experimentally measured in ref. [19]. Figures 1(c-e) present the amplitude distributions of the 3 components of the electric field E_x, E_y and E_z respectively while the figure 1(f) presents the total intensity distribution of the electric field. First, we can see that, at the cavity center, the E_y-component is maximum while the E_x- and E_z- components are zero.

Second, it is clear that the electric field components are spatially distributed differently along the major axis of the cavity i.e. a possible coupling to a NP should take into account the position of the latter as we will see later.

The magnetic field components are also given in figure 1(g-i) as well as its intensity in figure 1(j). As expected and because the cavity mode is an in-plane mode, H_z is predominant but its value vanishes at the cavity centre similarly to H_y while H_x is maximum. It may be mentioned here that, in the vertical direction (Oz), the cavity mode is located at the center of the InP membrane.

2.2. Study of the NP

As mentioned above, the considered spherical NP is designed so that it exhibits an ED resonance close to the wavelength resonance of the PCC mode. Thus, knowing the operation wavelength to be $\lambda_0^{mode} = 1602.92\ nm$, two solutions can be envisaged : (i) Fixing the radius R of the NP and changing its refractive index n_p, or (ii) Fixing the index and varying its radius. Nonetheless, if we want the coupling of the NP with the PCC to be local, we should consider the size of the NP smaller than the size of an electric or magnetic field lobe of the PCC mode (see figure 1(f)). This limits the choice to solution (i). From the distributions shown in figures 1(c-f), we estimate the size of this lobe to be about 440 nm (see the scale bar in figure 1(c)). Therefore, we fix the NP radius to be $R = 220\ nm$.

Using the Mie theory, we have calculated the spectral position of the ED resonance as

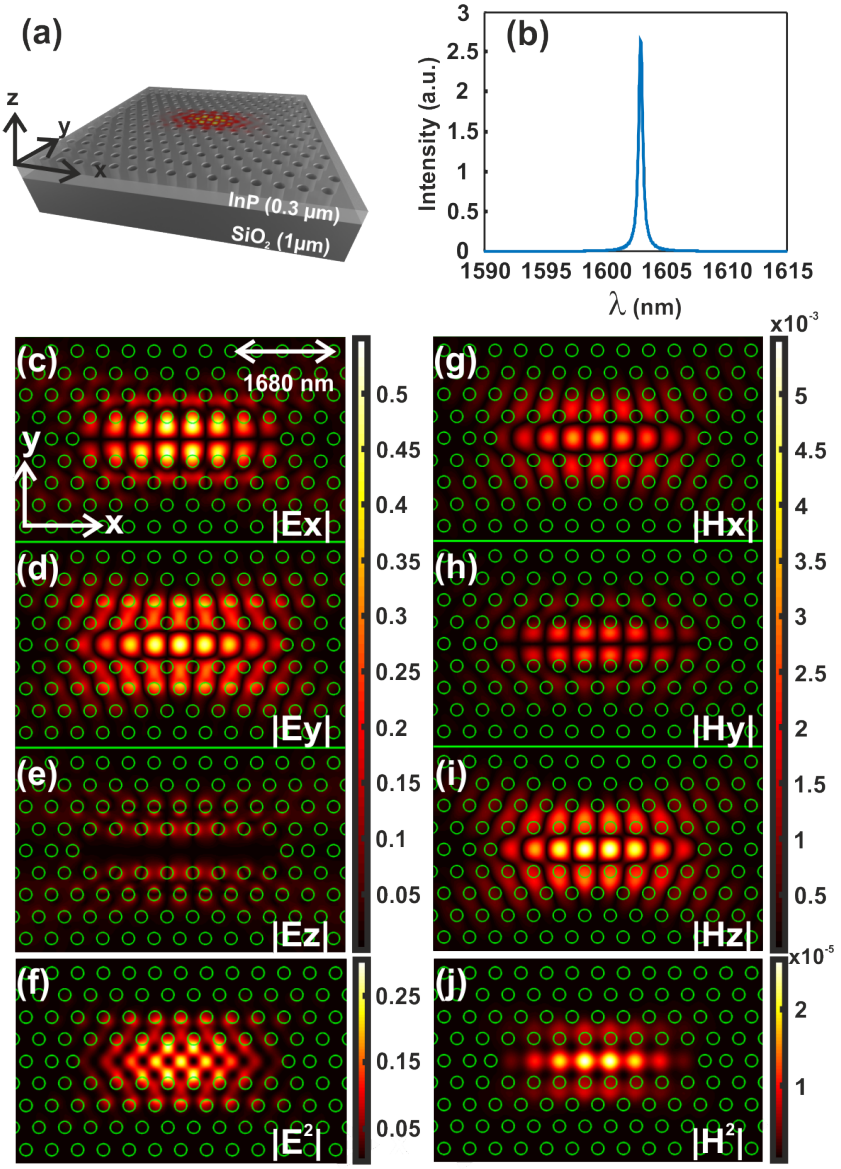

Figure 1: (a) Schematic of the considered PCC. (b) Near-field intensity spectrum calculated 15 *nm* in air above the center of the PCC. (c) to (e) and (g) to (i) are the amplitude distributions of the three components of the electric and magnetic field recorded at 15 *nm* above the PCC in air. (f) and (j) present the intensity distribution of the electric and magnetic field, respectively, recorded on the same plane as previously. Green circles show the position of the photonic crystal air holes.

a function of the refractive index of the NP (n_p). Figure 2(a) presents the obtained results providing the values of $n_p^{ED} = 4.85$ for the ED to be located at the PCC resonance wavelength. Note that this value of the refractive index does not necessarily correspond to a naturally existing material (even if $Re[\varepsilon_{GaAs}(\lambda = 450\ nm)] = 4.8427$) but it is needed to allow us understanding the physical effects related to the studied phenomenon. Figure 2(b) shows the effective scattering cross section (σ_S) spectrum

calculated using the Mie theory [22] (dashed line) in comparison with the one obtained by TFSF-FDTD [20] (solid line) algorithm that is described in the Appendix A. Indeed, this comparison helps to validate our FDTD codes which will be used in all the following simulations, especially for the study of the PCC-to-NP coupling. From figure 2(b), we see a fairly good agreement between the two results (see Appendix A for more information). Figures 2(c,d) show the distribution of the normalized electric field amplitude recorded respectively in the xz and yz planes passing through the center of the NP excited at the ED resonance wavelength.

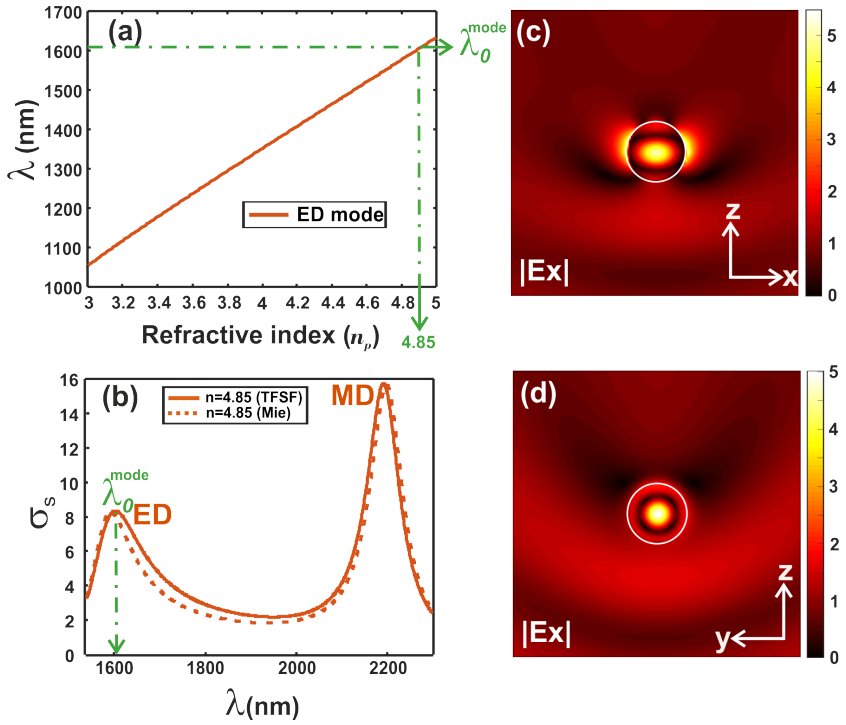

Figure 2: (a) Evolution of the spectral position (λ) of the ED mode as a function of the refractive index of a 220 nm radius NP. (b) Effective scattering cross section (σ_S) spectra corresponding to the NP with a refractive index ($n_p = 4.85$) indicated by the green arrow in (a) for which the ED wavelength is the same as the PCC resonance one. Two different numerical methods are used: the solid line correspond to the TFSF-FDTD method while the dotted line is calculated using Mie theory. (c,d) are the normalized electric field amplitude distributions recorded in the xz and yz planes respectively at the ED excitation. Note that the incident plane wave is propagating along the $z > 0$-axis and is linearly polarized along the x-direction.

2.3. Study of the NP-dielectric substrate coupling

The optical response of a resonator being strongly dependent on its environment [23,24], it is thus necessary to determine the influence of the presence of the InP substrate (without the cavity) as shown in figure 3(a) placed at a distance D_z from the NP on their

resonance properties. So, figure 3(b) shows the values of σ_S and the spectral position (λ_{ED}) of the ED excitation as a function of D_z. These results were obtained using an adapted TFSF-FDTD code taken into account the presence of the substrate. The illumination consists of a plane wave propagating from the substrate perpendicularly to the air-InP interface (see schematic of the system in figure 3(a)). As expected, a slightly small quasi periodic modification of σ_S along the z-direction occurs due to the presence of the interference pattern between the incident field and the small one reflected by the NP itself. This leads to a small modulation of the σ_S with a peculiar behavior in the near field where the coupling involves evanescent waves that are diffracted by the NP. We can notice that the oscillations appearing in the two curves are not synchronous even far from the substrate. This can be attributed to a geometrical effect (spherical NP) of the resonance contrary to that of a point dipole. Figures 3(c,d) present the normalized electric field amplitude distributions in the two vertical planes (xz and yz) that cross the center of the NP, when the latter is at $D_z = 45\ nm$ above the substrate for a ED excitation ($\lambda = 1624\ nm$). Let notice that, at this distance, the maximum of the electric field amplitude is enhanced compared to the case of the self-suspended NP (see figures 2(c,d)). This increase is accompanied by a large shift in the spectral position of the ED mode (up to 22 nm) when approaching the NP to the substrate, revealing the possibility of a tunable control of the PCC resonance wavelength for small PCC to NP distance as it will be shown in the following.

2.4. Study of the PCC-NP coupling and discussion

Let us describe the approach considered in order to achieve the main objective of this study that consists on demonstrating how the presence of NP can modify the pattern of light scattered by the cavity. Obviously, we have almost infinite possibilities for the spatial position of the NP with respect to the PCC. Consequently, we have made the choice to start from the center of the PCC, where the electric field intensity is maximum, and to move the NP along three perpendicular axis parallel to the z, x and y-directions respectively. Therefore, we will divide our study and discussion into two parts:

2.4.1. ***Part A: Near field, transmission and reflection*** We begin the study by determine the spectral behavior of the whole system resonance when the NP moves along the z-direction due to the fact that the coupling efficiency is more sensitive to the NP-to-PCC distance. Figures 4(a-c) show the evolution of the normalized spectra for: (a) the near-field "*NF*" (the normalized electric intensity recorded at 15 nm above the center of the PCC), (b) the transmission "*Tr*" (the normalized transmitted electric energy of the wave propagating to the far-field region along the $z > 0$), and (c) the reflection "*Refl*" (the normalized electric intensity of the wave propagating along the $z < 0$) as a function of the vertical position (D_z) of the NP. These quantities are calculated according to the equations below:

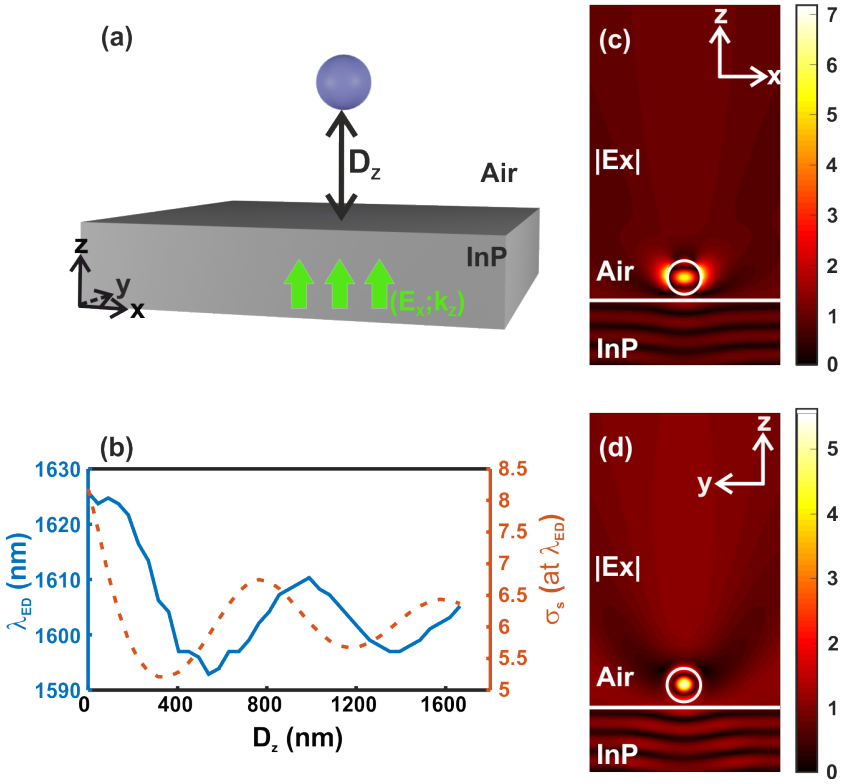

Figure 3: (a) Schematic of the considered configuration. (b) Variations of the ED spectral position (λ_{ED}) and the corresponding scattering efficiency (σ_s) of a NP (refractive index $n = 4.85\ nm$) coupled with an InP substrate ($n = 3.17$), as a function of the NP-substrate distance D_z. (c,d) are the electric field amplitude distributions recorded in the xz and yz planes at the ED excitation for $D_z = 45\ nm$.

$$NF = ||\overrightarrow{E}_d^{NF}(0,0,z_d)||^2 \tag{1}$$

$$Tr = \frac{\int\int_{-\infty}^{+\infty} ||\overrightarrow{E}_t(x,y,z_t)||^2 dx.dy}{\int\int_{-\infty}^{+\infty} ||\overrightarrow{E}_{inc}(x,y,z_t)||^2 dx.dy} \tag{2}$$

$$Refl = \frac{\int\int_{-\infty}^{+\infty} ||\overrightarrow{E}_r(x,y,z_r)||^2 dx.dy}{\int\int_{-\infty}^{+\infty} ||\overrightarrow{E}_{inc}(x,y,z_r)||^2 dx.dy} \tag{3}$$

Where : $||\overrightarrow{V}||$ is the modulus (norm) of the vector $\overrightarrow{V}$, $\overrightarrow{E}_d^{NF}(x_d, y_d, z_d)$ is the electric field vector recorded by a detector "d" placed at a distance "$z_d = 15\ nm$" above the center of the PCC ($x_d = 0, y_d = 0$), $\overrightarrow{E}_t(x,y,z_t)$ and $\overrightarrow{E}_r(x,y,z_r)$ are the diffracted zero-order of the electric field in the superstrate ($z_t > 0$) and the substrate ($z_r < 0$) respectively. $\overrightarrow{E}_{inc}$ is the same electric field vector calculated without the presence of the PC nor the NP.

As expected, a red shift of the resonance wavelength occurs for small distances accompanied by an enhancement of the light extraction in both substrate (reflection) and superstrate (transmission) regions. This result clearly demonstrates the possibility

to control the light extraction from the PCC by changing the NP position. Nonetheless, contrary to what was obtained for the NP alone, the maximum spectral shift of the PCC-NP resonance does not exceed 2.5 nm instead of 22 nm for the NP-substrate one. This is the signature of the great dominance of the PCC resonance even if the coupling is critical; predictable through the great value of its quality factor compared to that of the ED resonance of the NP alone. To go further, we have also studied the influence of the lateral position of the NP on the PCC resonance behavior. Figures 4(d-f) present the corresponding results when the NP moves along the x-direction parallel to the PCC major axis starting from its center while figures 4(g-i) correspond to a y-displacement of the NP along the perpendicular direction (PCC minor axis). In both cases, the NP vertical position was fixed to the $D_z = 45$ nm corresponding to a detector placed in air at 15 nm between the PCC and the NP. As can be seen, a strong modulation of the transmitted and the reflected intensity is obtained as a function of the position of the NP depending on whether it is above a maximum or minimum of the electric intensity of the cavity mode (see figure 1(f)). Moreover, we see on figures 4(e,f) that the minima of

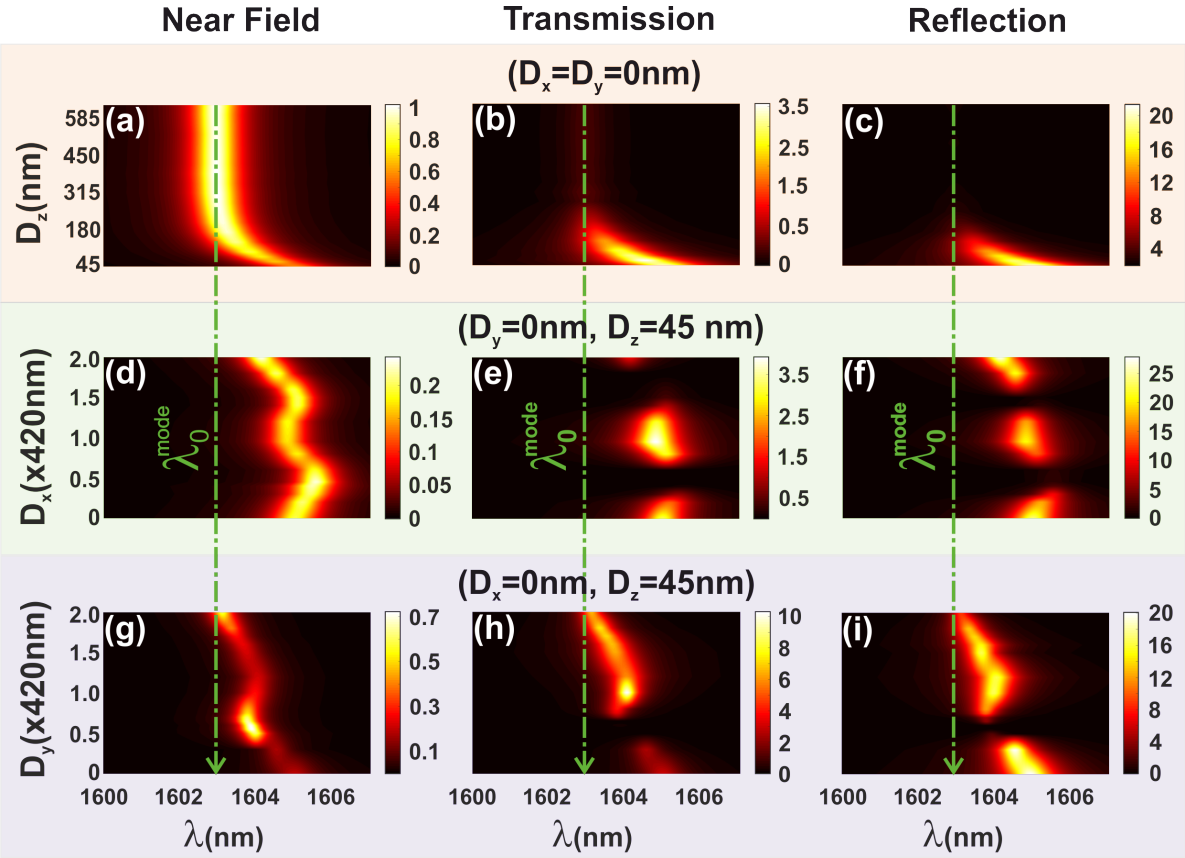

Figure 4: Normalized near-field (first column), transmission (second column) and reflection (third column) spectra of the PCC coupled to the NP ($n_p = 4.85$, $R = 220$ nm) as a function of its position along the (x, y, z) axes. The dashed green lines indicate the resonance wavelength (λ_0^{mode}) of the unperturbed PCC fundamental mode.

the transmitted and reflected intensities occur simultaneously and correspond to a total

extinction for $D_x = 0.5\ a = 210\ nm$ and $D_x = 1.5\ a = 630\ nm$. The same phenomenon also occurs when the NP moves along the y direction for $D_y = 0.5\ a = 210\ nm$ (see figures 4(h,i)). This implies that the energy is no longer scattered in the direction perpendicular to the structure otherwise the interpretation will be very difficult (along the z-axis) but in other directions which remain to be determined. Moreover, the same figures show that the maxima of transmission and reflection also occur simultaneously meaning that the energy flow is probably mainly directed along the vertical direction.

2.4.2. ***Part B: Radiation pattern*** In order to provide a clear and complete explanation on the modification of the emission, we have calculated the whole angular spectrum (see Appendix B) of the light emitted by the PCC alone as well as in the presence of the NP at different positions along both x and y directions in a plane located at $D_z = 45\ nm$.

In this part, we will impose that we are in the continuous wave (CW) regime which corresponds to the cavity mode frequency (i.e. without coupling) otherwise the interpretation will be very difficult.

In order to fully understand the light emission, we present the $4\pi\ sr$ radiation diagram of the PCC in figure 5 for four cases: in figure 5(a) we see that the angular spectrum of the energy scattered from the isolated PCC presents two lobes located by azimuth angle of $\phi = \pm 30°$ and directed outward from the vertical axis (z-axis) along almost $\theta = 31°$, while three lobes appear in the substrate side where two lobes oriented outward from the vertical axis along $\theta = 40.7°$. A third lobe exists and is directed vertically ($\theta = 0°$). When the NP is placed at position "A(0,0,45)" (see figure 5(b)), the scattered energy by the whole system (PCC+NP) is mainly directed in the vertical axis in transmission (air) and reflection (substrate) and its efficiency is about 1.79 times higher than that of the isolated PCC. Moving the NP to "B(630,0,45)" and "C(0,210,45)" positions leads to direct the scattered energy in special directions in the transmission and reflection regions, as shown in figure 5(c,d) with a slight enhancement of its efficiency to 1.1 times that of the isolated PCC. To have an overview, we made three videos that show the evolution of the angular spectra of the PCC-NP system according to the position of the NP. The movie "Movie1" shows this evolution when the NP moves vertically away from the center of PCC. The movies "Movie2" and "Movie3" show the evolution of the angular radiation spectra of the system when the NP is moved along the major axis of the PCC (x-axis) and along the minor axis of PCC (y-axis), respectively.

Through figures 4(a-c) and Movie 1, we can see that the PCC-NP coupling, where the NP moves vertically away from the cavity along the z axis, establishes two distinct cases of light extraction : for $D_z \leq 210\ nm$, the majority of the light is extracted vertically, whereas for larger distance, the coupling becomes increasingly weaker and thus the light scatters further away from the z-axis.

On the other hand, the lateral displacement of the NP leads us to the different interpretations. In the case of a displacement along the x-axis (movie 2), the light extraction behaves in 3 different aspects: When the NP is positioned above an intensity

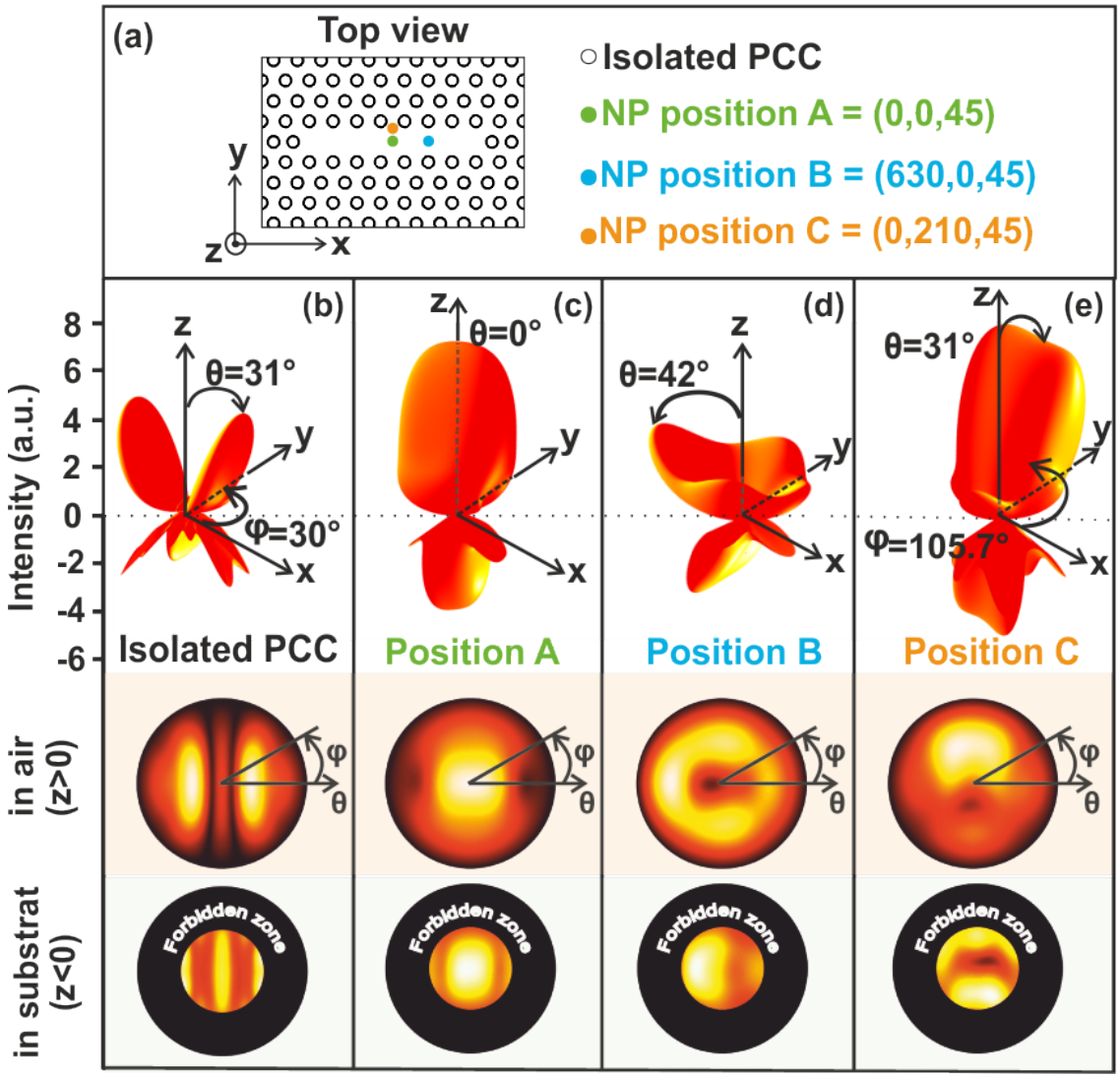

Figure 5: (a) Top-view of the PCC schema showing the three specific positions of the NP marked by 3 colored dots. 3D view of the total (4π sr) radiation angular spectra are shown in (b) for the isolated PCC, in (c) for the PCC-NP system when the NP placed 45 *nm* above the PCC center at position "A", in (d) for the PCC-NP system when the NP at position "B" and in (e) for the PCC-NP system when the NP displaced along the y-axis and placed at position "C". The 2D circular maps (see last two lines) give the angular spectra calculated in air (z>0) and in the substrate (z<0) for the four corresponding cases (isolated PCC, NP at A, at B and at C respectively).

maximum (see figure 1(f)), we see that the behavior of the extracted light is almost similar to the case of an NP placed above the center of the cavity (i.e., the majority of the light propagates vertically along the z-axis). When placed above an intensity minimum, the extracted light scatters in a quasi-isotropic shape with an extinction in the vertical direction leading to a "donut" form. In the third case presented by movie 3 (i.e. NP moving along the y-axis), the emitted light behaves differently from what

we got in the previous case. The variation of the direction of the extracted light is a bit irregular because the NP will pass over two different media (air and InP) when it moves. This irregularity is illustrated in figures 4(g-i) where there is only one position of the NP ($D_y = 0.5\ a = 210\ nm$) that causes an extinction of the light emitted in the vertical direction. This position appears clearly in figure 1(f).

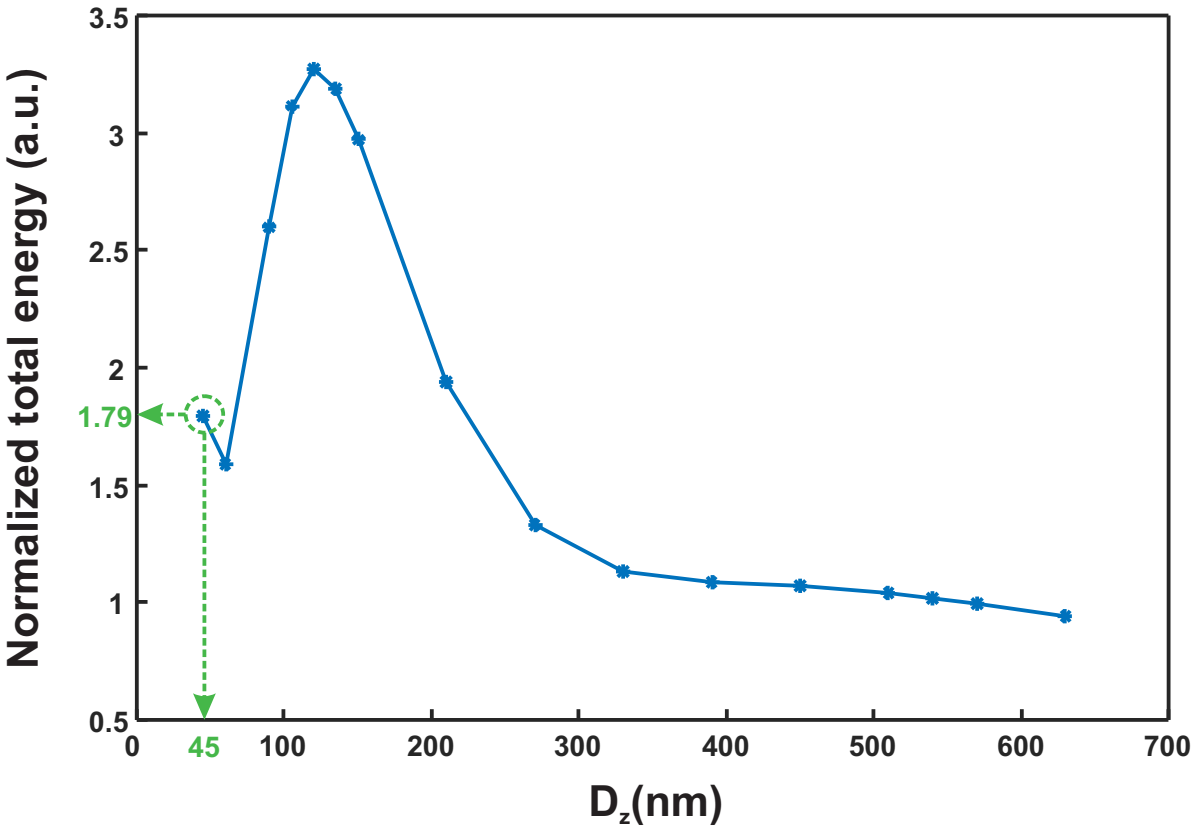

Figure 6: Normalized total radiated energy spectrum of the whole system (PCC+NP) as a function of the NP positions along the z-direction (D_z).

3. Conclusion

In summary, we present the effect of the coupling between a dielectric NP and an optical nanocavity exhibiting a same resonance wavelength. This results obtained demonstrate that this kind of coupling could offer a possible way to shape the angular radiation diagram of the whole structure. The weight and direction of the extracted light from the cavity can be tuned according to the NP position with respect to the cavity allowing a directive and selective emission into the substrate and/or the superstrate. We studied different configurations and showed that the coupling depends greatly on the near electromagnetic field distribution of the isolated nanocavity. When the ED resonant NP is over a maximum of the electric field, the coupling becomes strong and leads to an enhancement of the scattered light. Nevertheless, a particular position of the

NP along the z-direction could lead to a critical coupling for which the scattering is maximum. This phenomenon does not exist when the NP approaches a flat substrate. This is illustrated through an additional result that presents the total energy scattered over 4π sr as a function of the NP position. As illustrated in figure 6, this maximum is obtained for $D_z = 120\,nm$ in the case of our configuration. For other positions of the NP, its possible to direct the energy in a desired direction. For experimental demonstration, the position of the NP can be spatially controlled by sticking it on the apex of a SNOM tip for example, or by using optical tweezers in non contact regime such as in ref. [25]. The numerical tools developed in this work can be easily adapted to the study of any coupling between two optical nano-systems for the determination of their behavior in both near- and far-field regions.

Appendix A. Mie theory and TFSF-FDTD method

In our study, we used two calculation methods in order to determine the effective scattering cross-section (σ_S) of a spherical NP:
The first one is the well-known Mie theory that allows to calculate the coefficients related the each electric and magnetic multipoles through a spherical wave expansion of the scattered field. The weight of each component linked to a multipole (dipole, quadrupole, octopole...) is analytically calculated and its value allows to determine the nature of the excited resonance at a given wavelength. The total scattered energy is obtained by summing coherently all the fields and allows determining the scattering and the extinction optical cross sections. The ratio of the latter to the physical cross section of the NP allows determination of the effective extinction, absorption and scattering cross sections [22].

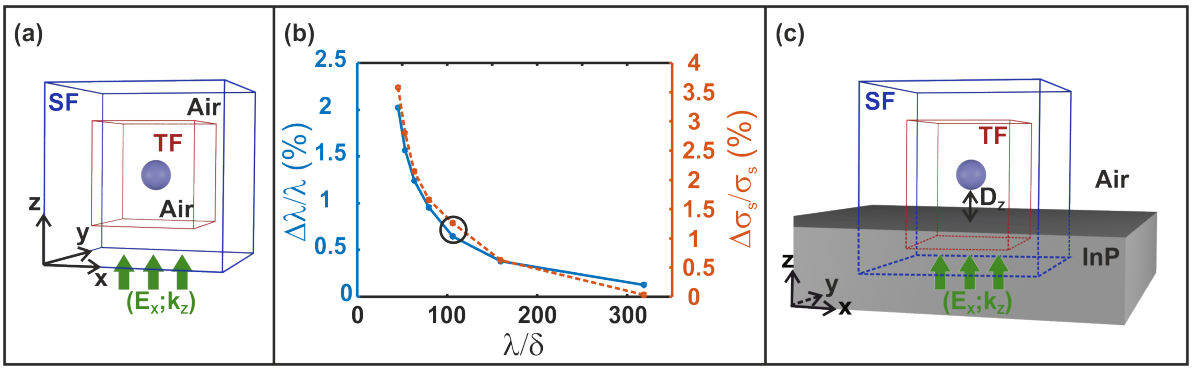

Figure A1: (a) Schema of a self-suspended NP in air and surrounded by the TF box (red box) and the SF box (blue box). (b) Relative deviation between the wavelength (blue curve) and the normalized scattering cross section (red curve) calculated by the FDTD code and Mie's theory as a function of λ/δ. (c) Schema of a NP suspended in air and placed at a distance D_z above an InP substrate. We can see the TF and SF boxes to penetrate into the substrate.

The second method is the so-called "Total Field - Scattered Field" (TFSF) technique associated to the FDTD (Finite Difference Time Domain) algorithm. The latter is based on spatial discretization of the structure under study through parallelepiped cells in the case of Cartesian coordinates. This kind of mesh is not well suitable to model structures with curved surfaces. Thus, in order to minimize an eventual stair-casing artifactual effect, several techniques were developed in the literature [26–29]. Nonetheless, in the case of a purely dielectric material without absorption, the averaging technique seems to be quite powerful. In this case, the dielectric constant of each cell, comprising two or more media of different dielectric constants, is calculated as the average value of the dielectric constant over the cell volume. We have tested this technique and demonstrated that it allows a very good agreement with Mie's theory as shown in next paragraph. The TFSF technique is based on a spatial division of the calculation window into two areas: the area of total field (TF) that contains the scatterers and where the calculated electromagnetic field consists on the sum of the incident and the scattered fields. For the second area, which encompasses the first one, only the scattered field (SF) is calculated by subtracting the incident field over all the external interface of the TF area at each temporal iteration. For a simple case where the NP is immersed in a homogeneous medium (see the figure A1(a)), we have compared the TFSF-FDTD results to the Mie theory ones (see figure A1(b)). This figure presents the variations of the relative deviation between the Mie and TFSF results for both the spectral position and the scattering efficiency as a function of the ratio λ/δ; δ being the FDTD cell size. As it can be shown, the results depends greatly on λ/δ and convergence only occurs when the cell size tends to zero. For our simulations, we set the cell size at $15 \times 15 \times 15$ nm^3 corresponding to a $\lambda/\delta = 107$ for which the deviation from the Mie theory is of only 0.8% (see figure A1(b)). Let notice that in the case of a substrate (figure A1(c)), the TFSF can be improved by subtracting not only the incident field but also the reflected one on the substrate interface [20,30]. We have developed and tested this configuration in view of obtaining the results presented in section 2.3.

Appendix B. Plane Waves Spectrum theory

The angular spectra of the radiation are calculated using the plane wave expansion (PWE) theory. This theory is based on the decomposition into an angular spectrum (i.e. as a function of the Euler angles θ and ϕ) through the known of the electric field $\overrightarrow{E}_P(x, y, z_0, \lambda)$ on a plane (P) parallel to xy one and located at $D_z = z_0$ (see figure B1). The PWE theory allows determining the electric field associated with each plane wave propagating along the (θ, ϕ) direction through:

$$\begin{aligned} \overrightarrow{E}(\theta, \phi, z_0, \lambda) &= \iint_{-\infty}^{+\infty} \overrightarrow{E}_P(x, y, z_0, \lambda) e^{-i\overrightarrow{k}.\overrightarrow{r}}\, dx\, dy \\ &= \iint_{-\infty}^{+\infty} \overrightarrow{E}_P(x, y, z_0, \lambda) e^{-i(k_x x + k_y y + k_z z_0)}\, dx\, dy \end{aligned} \tag{B.1}$$

With:

- $\overrightarrow{E}_P(x, y, z_0, \lambda)$ is the spatial distibution of the electric field in the plane (P)
- $\overrightarrow{k} = \begin{cases} k_x(\theta, \phi, \lambda) = \frac{2\pi n}{\lambda} \sin\theta \cos\phi \\ k_y(\theta, \phi, \lambda) = \frac{2\pi n}{\lambda} \sin\theta \sin\phi \\ k_z(\theta, \phi, \lambda) = \sqrt{(\frac{2\pi n}{\lambda})^2 - k_y^2 - k_x^2} \end{cases}$ are the wave vector Cartesian coordinates
- n is the refractive index of the medium in the (P) plane

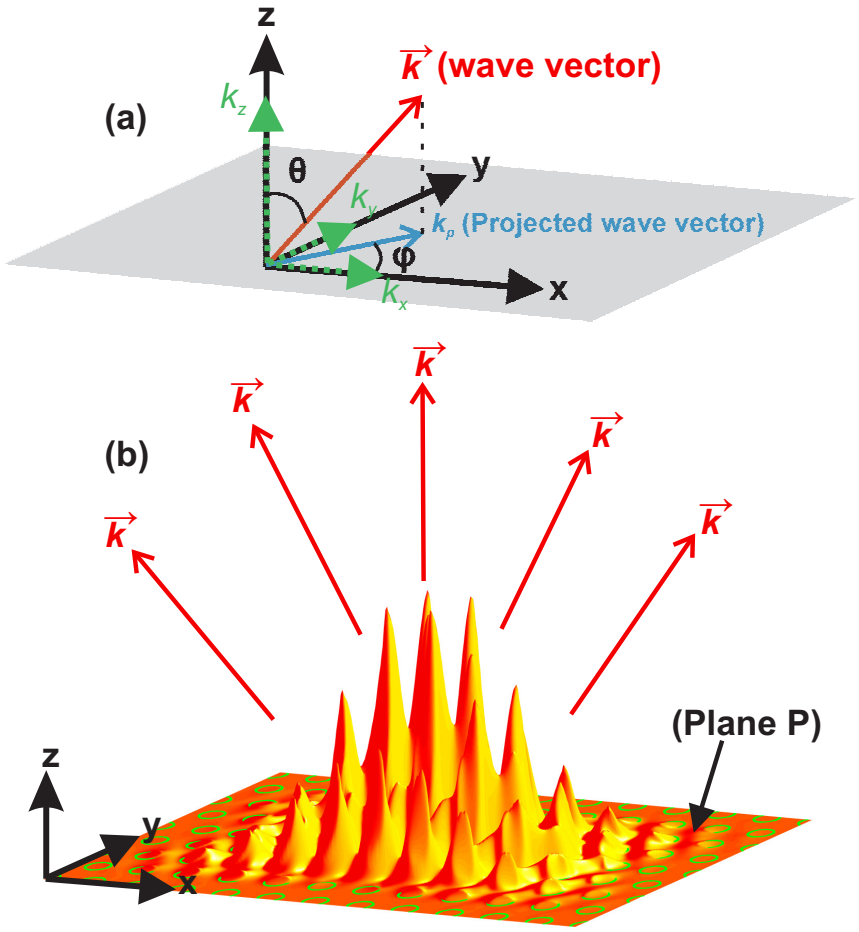

Figure B1: (a) Schematic of a wave-vector $\overrightarrow{k}$ located by its Euler angles (θ, ϕ) allowing the determination of its coordinates by simple projection. (b) 3D view of the electric field intensity distribution in the (P) plane. Green circles show the position of the photonic crystal air holes.

We note that the integration appearing in equation B.1 runs on the whole plane (P) from $-\infty$ to $+\infty$. This imposes to know the electromagnetic field everywhere in this plane. In practice, care must be taken to consider a sufficiently large calculation window corresponding to a field that cancels at the edges of the window. After the determination of the three components of the angular spectrum, we calculate the far field intensity by

considering the asymptotic limit given in [31, 32] by:

$$I(\theta, \phi, \lambda) = \lim_{z \to \infty} ||\overrightarrow{E}(\theta, \phi, z, \lambda)||^2 \propto \frac{-i}{\lambda} \cos\theta ||\overrightarrow{E}(\theta, \phi, z_0, \lambda)||^2 \tag{B.2}$$

where $||\overrightarrow{E}||$ is the modulus of the $\overrightarrow{E}$ field.

Acknowledgments

Computations have been performed on the supercomputer facilities of the "Mésocentre de calcul de Franche-Comté". This work has been partially supported by the EIPHI Graduate School (contract ANR-17-EURE-0002).

Data availability statement

All data that support the numerical results of this study are included within the article and appendixes.

ORCID iDs

F. I. Baida https://orcid.org/0000-0002-7475-525X

References

[1] K Bergenek, Ch Wiesmann, H Zull, R Wirth, P Sundgren, N Linder, K Streubel, and TF Krauss. Directional light extraction from thin-film resonant cavity light-emitting diodes with a photonic crystal. Appl. Phys. Lett., 93(23):231109, 2008.

[2] K Bergenek, Ch Wiesmann, R Wirth, L O'Faolain, N Linder, K Streubel, and TF Krauss. Enhanced light extraction efficiency from algainp thin-film light-emitting diodes with photonic crystals. Appl. Phys. Lett., 93(4):041105, 2008.

[3] Misha Boroditsky, TF Krauss, Roberto Coccioli, R Vrijen, R Bhat, and E Yablonovitch. Light extraction from optically pumped light-emitting diode by thin-slab photonic crystals. Appl. Phys. Lett., 75(8):1036–1038, 1999.

[4] Shanhui Fan, Pierre R Villeneuve, JD Joannopoulos, and EF Schubert. High extraction efficiency of spontaneous emission from slabs of photonic crystals. Phys. Rev. Lett., 78(17):3294, 1997.

[5] Misha Boroditsky, Rutger Vrijen, Roberto Coccioli, Raj Bhat, and Eli Yablonovitch. Spontaneous emission extraction and purcell enhancement from thin-film 2-d photonic crystals. J. Light. Technol., 17(11):2096, 1999.

[6] Amade Ndiaye, Ahlem Ghazouani, Christian Seassal, Emmanuel Drouard, Nicolas Olivier, and Badhise Ben Bakir. Enhanced light-extraction efficiency and emission directivity in compact photonic-crystal based algainp thin-films for color conversion applications. Opt. Express, 29(22):35965–35979, 2021.

[7] Svetlana V Boriskina, Trevor M Benson, Phillip Sewell, and Alexander I Nosich. Q factor and emission pattern control of the wg modes in notched microdisk resonators. IEEE J. Sel. Topics Quantum Electron., 12(1):52–58, 2006.

[8] Tim H Taminiau, Fernando D Stefani, and Niek F van Hulst. Enhanced directional excitation and emission of single emitters by a nano-optical yagi-uda antenna. Opt. Express, 16(14):10858–10866, 2008.

[9] CP Dettmann, GV Morozov, M Sieber, and H Waalkens. Directional emission from an optical microdisk resonator with a point scatterer. EPL (Europhysics Letters), 82(3):34002, 2008.

[10] Alexis Devilez, Brian Stout, and Nicolas Bonod. Compact metallo-dielectric optical antenna for ultra directional and enhanced radiative emission. ACS Nano, 4(6):3390–3396, 2010.

[11] Brice Rolly, Brian Stout, and Nicolas Bonod. Boosting the directivity of optical antennas with magnetic and electric dipolar resonant particles. Opt. Express, 20(18):20376–20386, 2012.

[12] Alexander E Krasnok, Constantin R Simovski, Pavel A Belov, and Yuri S Kivshar. Superdirective dielectric nanoantennas. Nanoscale, 6(13):7354–7361, 2014.

[13] Alec Rose, Thang B Hoang, Felicia McGuire, Jack J Mock, Cristian Ciracì, David R Smith, and Maiken H Mikkelsen. Control of radiative processes using tunable plasmonic nanopatch antennas. Nano Lett., 14(8):4797–4802, 2014.

[14] Davide Rocco, Luca Carletti, Andrea Locatelli, and Costantino De Angelis. Controlling the directivity of all-dielectric nanoantennas excited by integrated quantum emitters. J. Opt. Soc. Am. B, 34(9):1918–1922, 2017.

[15] Cheng-an Tao, Wei Zhu, Qi An, Haowei Yang, Weina Li, Changxu Lin, Fuzi Yang, and Guangtao Li. Coupling of nanoparticle plasmons with colloidal photonic crystals as a new strategy to efficiently enhance fluorescence. J. Phys. Chem., 115(41):20053–20060, 2011.

[16] Ehsan Eftekhari, Ivan S Cole, and Qin Li. The effect of fluorophore incorporation on fluorescence enhancement in colloidal photonic crystals. Phys. Chem. Chem. Phys., 18(3):1743–1749, 2016.

[17] Suli Wu, Hongbo Xia, Jiahui Xu, Xiaoqian Sun, and Xiaogang Liu. Manipulating luminescence of light emitters by photonic crystals. Adv. Mater., 30(47):1803362, 2018.

[18] Fadi I Baida and Thierry Grosjean. Double-way spectral tunability for the control of optical nanocavity resonance. Sci. Rep., 5(1):1–8, 2015.

[19] T Grosjean, A El Eter, M Mivelle, T-Ph Vo, A Belkhir, C Ecoffey, G Le Gac, D Nedeljkovic, A Rahmani, C Seassal, et al. Extraordinary blueshift of a photonic crystal nanocavity by reducing its mode volume with an opaque microtip. Appl. Phys. Lett., 101(5):051102, 2012.

[20] Allen Taflove, Susan C. Hagness, and Melinda Piket-May. Computational Electromagnetics: The Finite-Difference Time-Domain Method, pages 629–670. Elsevier Inc, December 2005.

[21] C Monat, C Seassal, X Letartre, P Regreny, Michel Gendry, P Rojo Romeo, P Viktorovitch, M Le Vassor d'Yerville, D Cassagne, JP Albert, et al. Two-dimensional hexagonal-shaped microcavities formed in a two-dimensional photonic crystal on an inp membrane. J. Appl. Phys., 93(1):23–31, 2003.

[22] Craig F Bohren and Donald R Huffman. Absorption and scattering of light by small particles. John Wiley & Sons, 2008.

[23] Elie M Atie, Tony Tannous, Thierry Grosjean, and Fadi I Baida. High optical resonance sensitivity to its environment of a fibered bowtie nano-aperture antenna. Appl. Phys. B, 120(4):581–586, 2015.

[24] Elie M Atie, Zhihua Xie, Ali El Eter, Roland Salut, Dusan Nedeljkovic, Tony Tannous, Fadi I Baida, and Thierry Grosjean. Remote optical sensing on the nanometer scale with a bowtie aperture nano-antenna on a fiber tip of scanning near-field optical microscopy. Appl. Phys. Lett., 106(15):151104, 2015.

[25] Nyha Hameed, Ali Nouho Ali, and Fadi I Baida. Optical manipulation of nanoparticles by simultaneous electric and magnetic field enhancement within diabolo nanoantenna. Scientific reports, 7(1):1–10, 2017.

[26] S Dey and R Mittra. A modified locally-conformal fdtd algorithm for modeling 3-d perfectly conducting objects. Microw. Opt. Technol. Lett., 17(6):349–352, 1998.

[27] Supriyo Dey and Raj Mittra. A conformal finite-difference time-domain technique for modeling cylindrical dielectric resonators. IEEE Trans. Microw. Theory Tech., 47(9):1737–1739, 1999.

[28] Wenhua Yu and Raj Mittra. A conformal fdtd algorithm for modeling perfectly conducting objects with curve-shaped surfaces and edges. Microw. Opt. Technol. Lett., 27(2):136–138, 2000.

[29] Rajagopal Nilavalan and Ian J Craddock. Interpolation/averaging in nonorthogonal fdtd

algorithm. Microw. Opt. Technol. Lett., 50(4):846–851, 2008.

[30] Dmitry L Markovich, Pavel Ginzburg, AK Samusev, Pavel A Belov, and Anatoly V Zayats. Magnetic dipole radiation tailored by substrates: numerical investigation. Opt. Express, 22(9):10693–10702, 2014.

[31] George C Sherman, Jakob J Stamnes, and Eamon Lalor. Asymptotic approximations to angular-spectrum representations. J. Math. Phys., 17(5):760–776, 1976.

[32] JJ Stamnes. Waves in focal regions hilger. Bristol, UK, 1986.